Journal of Environmental Chemical Engineering 11 (2023) 110677

Contents lists available at ScienceDirect

Journal of Environmental Chemical Engineering

journal homepage: www.elsevier.com/locate/jece

Bioapatite derived from animal bones as support for environmentally concerned catalysts: WGS with suppressed methanation activity

Unai Iriarte-Velasco [a], Irene Sierra [a,*], Miguel A. Gutiérrez-Ortiz [b], Jose L. Ayastuy [b]

[a] Department of Chemical Engineering, Faculty of Pharmacy, University of the Basque Country UPV/EHU, Paseo de la Universidad, 7, 01006 Vitoria, Spain
[b] Department of Chemical Engineering, Faculty of Science and Technology, University of the Basque Country UPV/EHU, Barrio Sarriena, s/n, 48940 Leioa, Spain

ARTICLE INFO

Editor: Apostolos Giannis

Keywords:
Bone char
Bioapatite
Nickel
WGS
K_2CO_3
H_2SO_4

ABSTRACT

The potential of natural apatite derived from pork bones to be used as a support of Ni catalysts for the Water-Gas Shift (WGS) reaction was investigated. Samples of bone char were chemically treated with either K_2CO_3 or H_2SO_4 and subsequently heated in inert or oxidizing atmosphere at various temperatures. Catalysts were characterized by ICP-AES, N_2 physisorption, XRD, FTIR, TG-DTG, H_2-TPR, XPS, H_2 chemisorption and NH_3-TPD, and tested in the WGS reaction, using both ideal and realistic (mixture of H_2O, CO_2 and H_2) feed streams. Nickel was partly exchanged with Ca^{2+} ions in the support. Regarding the effect of the atmosphere, an inert atmosphere had a negative effect due to the collapse of the porous structure. On the contrary, the combination of an oxidizing atmosphere and treatment with K_2CO_3 allowed a superior WGS performance under real reformer conditions, with a substantial decrease in the methane formation (six-fold decrease, compared to the non-activated reference catalyst). The catalytic activity could be related to the apatitic phase growing geometry, which can be tailored by the activation method.

1. Introduction

The use of energy sources alternative to fossil fuels, such as hydrogen, would contribute to the development of green economy, an economy that aims for sustainable development without degrading the environment. The success of the hydrogen economy depends on the availability of a sustainable and economic way to produce hydrogen, and its transformation into energy [1,2]. The steam reforming of hydrocarbons is a mature catalytic technology to produce H_2 [3,4], which can be used to feed fuel cells, providing electricity with zero emissions. In the current state of the art of fuel cells technology, the hydrogen stream must be purified in order to reduce the CO content to below 50 ppm [5]. Water-Gas Shift (WGS) is one of the most important reactions in the hydrogen production process [6,7]. WGS is the first step to produce a reformer gas with a reduced CO content. The fact that WGS is exothermic obliges to set up two reaction steps, a high-temperature WGS (350–500 ºC) followed by a low temperature WGS (190–250 ºC), in order to take advantage of both the reaction kinetics and thermodynamics.

In the search for alternative catalytic systems, excellent WGS activity has been reported for precious metals (Au, Ru) supported on hydroxyapatite (HAp) [8]. Miao et al. [9] reported stable and near equilibrium CO conversions over Pt supported on hydroxyapatite without CH_4 formation up to 450 ºC. They found a correlation among the activity and the Ca/P ratio of the support, suggesting that the apatite surface chemistry has a relevant effect in the WGS catalysis. It has been proposed that water molecule can be strongly activated on the apatite surface through the simultaneous coordination to Lewis acidic Ca^{2+} cations and H-bonding to basic O atoms of phosphate groups or other oxygen-containing groups [10,11].

As an alternative to the use of synthetic HAp, the thermochemical conversion of waste animal bones can be used to produce a biochar that contains mainly bioapatite, together with carbon and other substances [12–14]. Animal waste bones have been traditionally thrown away as waste. At present, over 140 M pigs are reared across the European Union (EU), which represents the largest livestock category [15].

In an earlier study we explored the utilization of the biogenic apatite obtained from the thermal treatment of pig bone as a support for WGS catalysts based on transition metals [16]. Compared to the limited availability of noble metals, catalysts based on transition metals are more attractive for industrial application due to their high catalytic activity and lower cost [17]. According to the results, using an ideal feed mixture (CO/H_2O = 1/2) the catalytic activity of various metals

* Corresponding author.
E-mail address: irene.sierra@ehu.eus (I. Sierra).

https://doi.org/10.1016/j.jece.2023.110677
Received 17 May 2023; Received in revised form 14 July 2023; Accepted 28 July 2023
Available online 29 July 2023

supported onto bone char varied as follows: Ni > Co > > Cu > Fe, thus being Ni the most active catalyst [16]. Despite their low cost and high catalytic activity, Ni based catalysts have not been extensively used in WGS reaction, as nickel catalyzes the undesired reaction of methanation [18]. This side reaction (among others) can lead to catalyst deactivation by coke deposition [19]. Moreover, Ni based catalysts may undergo metal particle sintering [20].

Consequently, it is essential to configure a catalyst with a limited methanation activity. The catalytic support influences the catalytic behaviour of the catalyst, since it affects both the metal-support interaction and the stability. In this regard, the utilization of natural apatite as support reduced the methane formation by around ten fold, as compared to a Ni catalyst supported onto synthetic HAp [16]. The results showed that the most active Ni catalyst (5 wt %) provided a 87 % CO conversion with a very low methanation activity (Y_{CH4}=0.25 % at 450 ºC), using an ideal feed mixture. This is an important advantage of using bioapatite supports, since the methanation reaction can significantly lower the efficiency of WGS [21]. Furthermore, the ion exchange ability of bioapatite support allows the incorporation of Ni into the lattice, thus favouring the metal-support interaction, which leads to an improved stability of Ni particles against sintering.

In a subsequent work [22], the activity of the catalysts supported on bioapatite was further improved by increasing the Ni loading (10 wt %), reaching a near equilibrium CO conversion (i.e. 92 % at 375 ºC), with still a limited methane yield (Y_{CH4} = 1.8 %) using an ideal feed mixture. The electronic band structure of the metal-bioapatite system was associated with an enhanced capacity for the oxidation of CO instead of the recombination with the adsorbed proton to form methane. However, using a typical reformer gas composition ($CO/H_2O/CO_2/H_2$ = 6/46/4/31), the selectivity to hydrogen was deteriorated since the methanation activity dramatically increased to around 60 %, with a negative net hydrogen production.

The physico-chemical properties of the bioapatites used as support, such as bulk and surface composition and textural properties, can significantly affect the catalytic behaviour of the catalyst, including the conversion and the methanation activity. For example, the relative amount of Ca^{2+}, OH^- and PO_4^{3-} in the bulk and surface of apatite may affect its acid properties, and also the exchange capacity of the loaded metal, which can eventually affect the speciation of the metal in the catalyst [23,24].

The physicochemical properties of bioapatite can be modified by chemical activation. However, a literature review shows that the number of studies focused on the effect of the chemical activation of bioapatite on its catalytic performance is scarce. Most of the investigations available in the literature dealing with the chemical activation of bones are focused on the adsorption properties of the developed material [25–27]. As an example of one the few works on this issue, Amiri et al. [28] investigated the chemical activation of waste bones with hydrogen peroxide. The chemically activated biochar became more thermally stable. Moreover, the exchange between Co^{2+} and Ca^{2+} into the bioapatite framework favoured the incorporation of Co as catalytic active phase for the degradation of dyes.

Herein, chemical activation was used to prepare suitable and sustainable catalytic supports for the WGS reaction from waste animal bones. To the best of our knowledge, there is no study regarding the WGS activity of catalysts supported on bioapatite, prepared through the modification of its physico-chemical properties by chemical activation. The treatment consists of the impregnation with either K_2CO_3 or H_2SO_4, and the subsequent heating in oxidizing or inert atmosphere, at various temperatures. The obtained biochars were loaded with Ni and the prepared catalysts were thoroughly characterised (N_2 physisorption, XRD, FTIR, ICP-AES, TG-DTG, H_2-TPR, XPS, H_2 chemisorption, NH_3-TPD) and tested in the WGS reaction.

2. Materials and methods

2.1. Catalyst synthesis

The support was prepared from pork chop bones collected from a local butcher shop. First, bones were cleaned from meat, cut into pieces of 2–5 cm and precalcined in air flow (120 NmL/min), heating at 5 °C/min to 500 °C and hold for 2 h. The obtained biochar was sieved and particles in the 0.09–0.25 mm size range were selected. This material will be referred as precursor (HAp).

The precursor was modified by chemical treatment using either H_2SO_4 (S) (at 0.2 $mmol_{H2SO4}/g$) or K_2CO_3 (K) (at 5 $mmol_{K2CO3}/g$). These ratios were set based on our previous experience [13]. The samples were dried in an oven overnight at 105 ºC. The subsequent heating was carried out at 10 ºC/min in either oxidative/calcination (air, A) or inert/-pyrolysis (nitrogen, N) conditions at two temperature levels (HTT, highest treatment temperature) for each atmosphere, holding HTT for 120 min. These HTT (350 and 550 ºC for the oxidizing atmosphere, and 600 and 800 ºC for the inert atmosphere) were established based on the weight-loss profile of the impregnated precursor (Fig. S1, Supplementary material). Various supports (detailed in Table S1, Supplementary material) were prepared and coded. For instance, KA350 refers to the biogenic precursor impregnated with K_2CO_3 (K) and calcined in air atmosphere (A) at a HTT of 350 ºC.

Ni was loaded onto the aforementioned supports by wet impregnation. For the preparation, 2.0 g of $Ni(NO_3)_2{\cdot}6H_2O$ (Aldrich) were dissolved in milli-Q water (10 mL) and impregnated onto the activated precursor samples (3.5 g) in a rotavapour device. These catalysts were named preceding Ni. For comparison purposes, Ni was also loaded onto the unmodified precursor (Ni/HAp). The obtained solids were calcined at 450 °C for 2 h (10 °C/min, in air flow).

2.2. Catalyst characterisation

The bulk chemical composition of the solids was evaluated by ICP-AES. Brunauer-Emmett-Teller (BET) method was used to determine the specific surface area, whereas the average pore size, total pore volume and pore size distribution (PSD) were estimated based on the Barrett, Joyner & Halenda method (BJH) from the data of N_2 desorption branch. The thermogravimetric analysis of the chemically treated samples was performed to measure the weight loss and its rate.

The crystalline structure of the support and the catalysts was analyzed by XRD using the International Centre of Diffraction Data (ICDD) database for the identification of the phases. The Rietveld method was used for microstructure analysis (profile refinement) and for the estimation of unit cell parameters. The crystallinity of the solids was assessed by the Crystallinity Index (CI), calculated from the full width at half maximum of (002) reflection [29]. The reducibility and metal speciation of the catalysts were examined by temperature-programmed reduction (H_2-TPR).

Fourier transform infrared spectroscopy (FTIR) transmission spectra for the calcined solids were recorded using disks of samples diluted in KBr. X-ray photoelectron spectroscopy (XPS) analysis was performed for both calcined and reduced forms of the solids. The peaks were deconvoluted after Shirley background subtraction, using a mixed Gaussian–Lorentzian function.

The surface acid sites were characterized by means of the chemisorption of ammonia pulses and the subsequent NH_3-TPD. The total acidity was calculated from the integration of the pulses, and the strength of the acid sites was evaluated from the corresponding TPD profile.

More details on analytical methods are given in Supplementary material.

2.3. Catalytic performance

The WGS performance was studied in a downflow fixed bed stainless steel reactor (D_i = 13.3 mm; length = 305 mm). Prior to the reaction, the catalyst (0.1 g diluted in silicon carbide particles of the same size, to achieve 1 mL) was reduced in H_2/He flow (15 vol % of H_2) at 400 °C for 1 h. Then, the reactor was cooled down to 200 °C in He flow and the feed stream was introduced. Deionized water was supplied by a HPLC pump (Gilson 307), and vaporized at 150 ºC before mixing with the reactant gases. Catalyst activity tests were carried out at atmospheric pressure in the 250–450 ºC range, with a total flow rate of 200 mL/min STP (GHSV=120,000 h^{-1}). Two different feed compositions were tested: (i) CO/H_2O/He (in vol %): 1/2/97, representative of an ideal WGS mixture; and (ii) $CO/H_2O/CO_2/H_2$/He = 5/46/4/31/14, representative of a realistic reformer outlet stream. A Peltier device was used to condense the unreacted water from the reactor outlet stream before routing the non-condensable products to an Agilent μGC (two molecular sieves with He and Ar carriers, respectively, and one PPQ column with He carrier) equipped with a TCD detector. Samples were collected once steady state at each temperature was attained. Stability tests (24 h of duration) were conducted under realistic WGS feed composition.

The CO conversion and yields (Y_i) to H_2 and CH_4 were calculated according to Eqs. (1)–(3):

$$X_{CO}(\%) = 100 \times \frac{F_{CO,in} - F_{CO,out}}{F_{CO,in}} \quad (1)$$

$$Y_{H2}(\%) = 100 \times \frac{F_{H2,out} - F_{H2,in}}{F_{CO,in}} \quad (2)$$

$$Y_{CH4}(\%) = 100 \times \frac{F_{CH4,out}}{F_{CO,in} + F_{CO2,in}} \quad (3)$$

3. Results

3.1. Catalysts characterisation

3.1.1. Textural properties and chemical composition

The reference catalyst (Ni/HAp) showed a S_{BET} of 70.8 m^2/g, a pore volume (V_{pore}) of 0.29 cm^3/g and an average pore diameter (d_{pore}) of 15.1 nm (Table 1). These values were notably modified during the activation of the support (S_{BET}: 2.0–90.9 m^2/g; V_{pore}: 0.001–0.310 cm^3/g; d_{pore}: 11.1–48.0 nm). The pore size distribution of the obtained solids (Fig. 1) showed the typical hierarchical pore distribution of bone chars [30,31] with two main intervals: (i) at small mesopore range (2.0–3.5 nm); and (ii) at large mesopore range with peaks at different values depending on the treatment (i.e. at around 6, 8, 20 and 30 nm). The results (Fig. 1A) showed that the chemical treatment followed by heating in air atmosphere at mild conditions (see Ni/KA350, Ni/SA350 vs. Ni/HAp) increased both the amount of mesopores and specific surface area. This effect was more important for the catalysts prepared by acid treatment, which might wipe off the inorganic compounds of biochar. A further increase in the HTT from 350 to 550 ºC caused a drastic removal of small mesopores (d_{pore}: 2–20 nm) along with the generation of new macropores. Consequently, the average pore size increased (from 14 to 30 nm, Ni/KA350 vs Ni/KA550; from 11 to 25 nm, Ni/SA350 vs Ni/SA550). Concomitantly, the S_{BET} dropped by a half.

Table 1
Textural and chemical characteristics of catalysts of Ni supported on bone char.

Catalyst	S_{BET} (m^2/g)	d_{pore} (nm)	V_{pore} (cm^3/g)	Ni (wt %)*	Ca/P ratio (at./at.)*
Ni/HAp	70.8	15.1	0.29	11.3	1.44
Ni/KA350	77.5	13.6	0.30	10.0	1.46
Ni/KA550	33.2	30.0	0.25	9.7	1.48
Ni/KN600	14.5	28.3	0.06	9.9	1.48
Ni/KN800	2.0	48.0	0.01	9.8	1.48
Ni/SA350	90.9	11.1	0.30	10.0	1.42
Ni/SA550	45.7	25.4	0.31	9.7	1.45
Ni/SN600	36.6	32.5	0.30	9.7	1.44
Ni/SN800	9.5	19.1	0.04	10.0	1.45

* ICP analysis

The thermal treatment under inert atmosphere (Fig. 1B) had a negative effect on the textural properties and caused the collapse of the pore structure. At a comparatively similar HTT, it yields catalysts with 20–56 % lower S_{BET} values.

In our samples, the measured Ca/P ratio was around 1.44 for the reference Ni/HAp catalyst and varied in the 1.42–1.48 for the rest of samples (Table 1). Slightly higher Ca/P values were obtained by the K treatment (Ca/P = 1.46–1.48) while S treatment led to lower ratios (1.42–1.45). These Ca/P values were in-between the stoichiometric hydroxyapatite (1.67) and brushite (1.0) and, in line with XRD data, suggest that calcium-deficient hydroxyapatite was formed by the charring of animal bones [32]. The relatively high concentration of heteroatoms (K, Na, N) in natural apatite is noteworthy (Table S2, Supplementary material), which is a distinctive characteristic from the synthetic hydroxyapatite [33]. Indeed, the presence of minor constituents evidence the substitution of calcium sites in the apatite lattice.

3.1.2. Structural characterisation

The XRD measurements revealed that the precursor was a solid with poor crystallinity (CI = 0.50, Table 2). The diffraction patterns of the prepared catalysts (Fig. S3, Supplementary material) were consistent with apatite phase (ICDD 01–84–1997) with the main characteristic diffraction peaks at 2θ= 31.993°, 32.230°, 31.844° and 25.886° clearly identified.

The XRD pattern of samples obtained after treatment at low HTT (350 ºC) displayed similarities with the reference catalyst (CI = 0.50–0.52 for Ni/HAp, Ni/KA350 and Ni/SA350 catalysts). As could be expected, after a more severe thermal treatment (HTT ≥ 550 ºC), independent of the heating atmosphere, the peaks became more intense and sharper. Apatite crystallite size (d_{HAp}) increased with HTT (Fig. S4, Supplementary material), as well as the CI, which increased up to 0.72–0.73 for the highest HTT. Moreover, upon heating in nitrogen at 800 ºC, new peaks emerged at ~31.5º and ~35º 2θ, characteristic of whitlockite ($Ca_{18}Mg_2H_2(PO_4)_{14}$, ICDD 01–70–2064).

Intriguingly, the chemical treatment with K_2CO_3 favoured the apatite crystal growing, as deduced from both XRD data. For instance, at HTT = 550 °C in air atmosphere, the apatite crystal size was 40 nm for the catalyst based on K_2CO_3-treated biochar, whereas it was 25 nm for the catalyst based on H_2SO_4-treated biochar. Similarly, for samples heated in inert atmosphere, the K_2CO_3 treatment resulted in an average crystal size of 53 nm (at HTT = 600 ºC), two fold larger than the acid treated counterpart (23 nm at HTT 550 ºC). The small difference in the HTT, a priori, is not enough to explain such difference. It is also interesting to note that as crystallinity was developed (d_{HAp} > 25 nm), a strong inverse correlation exists between S_{BET} and apatite crystallite size (Fig. 2). Contrarily, among samples with low crystal growth no correlation was observed, and a high variance in the S_{BET} could be observed, what was ascribed to an intensified effect of the applied chemical treatment.

The Rietveld refined lattice parameters of the precursor (a = 9.40809 Å, c = 6.8783 Å) were in-between those of pure hydroxyapatite (a = 9.4180 Å, c = 6.884 Å, ICDD 00–009–0432) and chlorofluoroapatite (a = 9.3973 Å, c = 6.8782 Å, ICDD 01–084–1997), which reflects the flexibility of natural apatites regarding the presence of

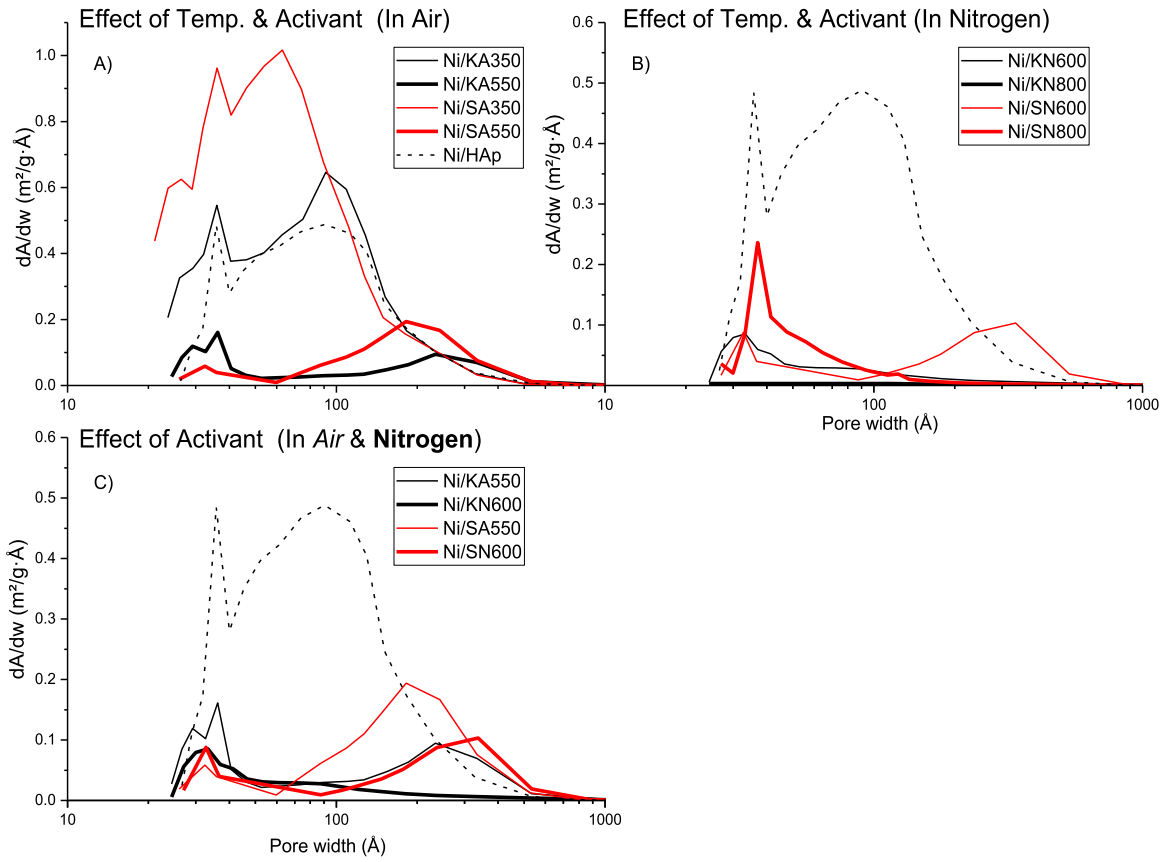

Fig. 1. PSD of the synthesized catalysts. A) Effect of HTT and activating agent in air (low HTT thin line; high HTT thick line); B) Effect of HTT and activating agent in pyrolysis conditions and C) Effect of activating agent (H_2SO_4 red; K_2CO_3 black). For comparison purposes, PSD of support, before metal impregnation, is shown by dashed lines. Prior to the N_2 adsorption-desorption, the sample was degassed at 300 ºC for 10 h under He flow.

Table 2
XRD characteristics of catalysts of Ni supported on bone char.

Catalyst	CI	*a* (Å)	*c* (Å)	Volume (nm^3)	$r_{c/a}$	d_{HAp} (nm)	d_{NiO} (nm)
Ni/HAp	0.50	9.41307	6.87643	0.52766	0.94	24	7 (n.d.)
Ni/KA350	0.52	9.41093	6.87854	0.52758	1.03	27	14
Ni/KA550	0.57	9.41008	6.88123	0.52770	0.83	40	13 (16)
Ni/KN600	0.70	9.41503	6.88458	0.52851	0.71	53	9
Ni/KN800	0.72	9.41401	6.88121	0.52813	0.52	93	10
Ni/SA350	0.50	9.41644	6.87673	0.52806	0.97	26	9 (10)
Ni/SA550	0.60	9.42095	6.87947	0.52878	0.93	25	17 (21)
Ni/SN600	0.62	9.42069	6.87822	0.52865	0.85	23	14 (26)
Ni/SN800	0.73	9.42663	6.87698	0.52923	0.51	75	7

In brackets the crystallite size of metallic Ni after reduction in H_2 flow at 400 °C.

different ions [34,35]. Indeed, biological apatites differ chemically from stoichiometric HAp in that they contain additional elements substituted into the HAp lattice. Table S2 (Supplementary material) indicates the presence of ions such as Cl^-, Na^+ and Mg^{2+}.

The lattice dimensions increased after Ni impregnation and the subsequent heating, which may be related to the substitution of Ca^{2+} in the apatite structure by Ni^{2+}. Moreover, the chemical impregnation also resulted in an alteration of the lattice dimensions: K_2CO_3 led to a more marked expansion in the *c* axis, whereas for H_2SO_4 the expansion was higher in the *a* axis. These results could be attributed to the incorporation of several species into the apatite lattice by ion exchange, such as K^+ and SO_4^{2-}. The results of Table S2 confirmed a small amount of S in the samples treated with H_2SO_4 (absent in both the precursor and samples treated with K_2CO_3), as well as an increase in the amount of K in the samples treated with K_2CO_3.

The intensity ratio ($r_{c/a}$) of diffraction patterns corresponding to apatite (002) (*c*-axis) and (300) planes (*a*-axis) was used to calculate the dominant growing plane of the apatite crystals. $r_{c/a}$ values (summarised in Table 2) showed that the acid or alkali treatment and the HTT clearly conditioned the crystal growth, providing anisotropic characteristics to the obtained bioapatite. Two main behaviours can be outlined; (i) $r_{c/a}$ was higher for air-heated samples, that is, the calcination in air atmosphere may favour the crystal growth predominantly in the *c*-axis; and (ii) as HTT increased, the apatite crystallites grew preferentially in the *a*-axis orientation, as suggested by the lower $r_{c/a}$ values. The actual nickel loading of the catalysts (Table 1) was very close to the nominal value of 10 % for all catalysts, which corresponded to around 1–3 times the theoretical monolayer amount for the supports calcined in air, and above ten-fold for the supports activated in pyrolysis conditions (exception Ni/SN600, for which 3). This situation could anticipate a larger dispersion in the air-calcined series. However, NiO nanoparticle size measured from XRD analyses (Table 2) reflected the opposite

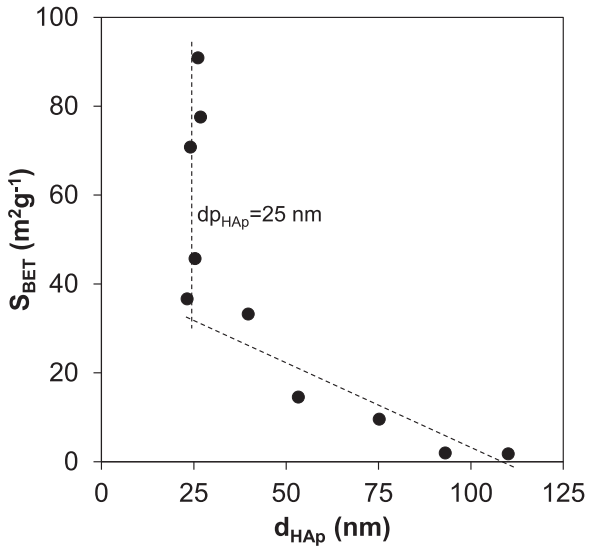

Fig. 2. Specific surface area of chemically activated Ni/HAp catalysts against apatite crystal size.

behaviour. For instance, the precursor of Ni/KA550 catalyst contained NiO particles of around 13 nm whereas Ni/KN600, charred even at a higher temperature, contained smaller ones of around 9 nm. These results suggest that, in addition to the Ni loading, the $r_{c/a}$ parameter could also determine the NiO crystal size, indicating that heating in air atmosphere favoured the NiO crystallite growth.

3.1.3. Redox properties

The effect of the chemical activation of the precursor on the reducibility of the Ni species is shown in Fig. 3. The hydrogen uptake of the selected catalysts started at around 200 ºC and several hydrogen consumption peaks could be identified. The H_2-TPR profile was deconvoluted into five hydrogen consumption events (Fig. S5, Supplementary material). The peak at around 250 ºC (α-peak) was ascribed to the reduction of surface oxygen species in bioapatite [31,36]. The reduction of NiO oxides was divided into three temperature ranges in the 300–500 ºC range. The peak at around 300 ºC (β1-peak) was attributed to easily reducible, small NiO particles with weak interaction with the support [37,38]. The peak from 370-400 ºC (β2-peak) was assigned to the reduction of species having mild interaction with the support (for instance, the NiO particles previously identified by XRD). However, the subtle right shoulder, denotes that it could also include the reduction of some less reducible species, such as $Ni^{\delta+}$ in the apatite [39]. The intensity of this band notably varied with the activation treatment and it represented the main hydrogen consumption for all the investigated catalysts. The reduction peak at 450–500 ºC (γ1-peak) was attributable to species with strong interaction with the support, likely ion exchanged Ni^{2+} in the Ca^{2+} sites of the apatite [39–41]. Finally, the hydrogen consumption at high temperatures was ascribed to the dehydroxylation of the apatitic support (γ2-peak) [42]. Note that the bone char used as precursor was stabilised at 500 ºC. It is worth mentioning that the hydrogen consumption in the reference catalyst Ni/HAp and Ni/SA350 catalyst largely exceed the stoichiometric value, and thus, suggested that the dehydroxylation of the support took place. Also, the occurrence of carbon gasification reactions (i.e. reaction between C in bone char and hydrogen to produce methane) should not be discarded at high temperatures [43].

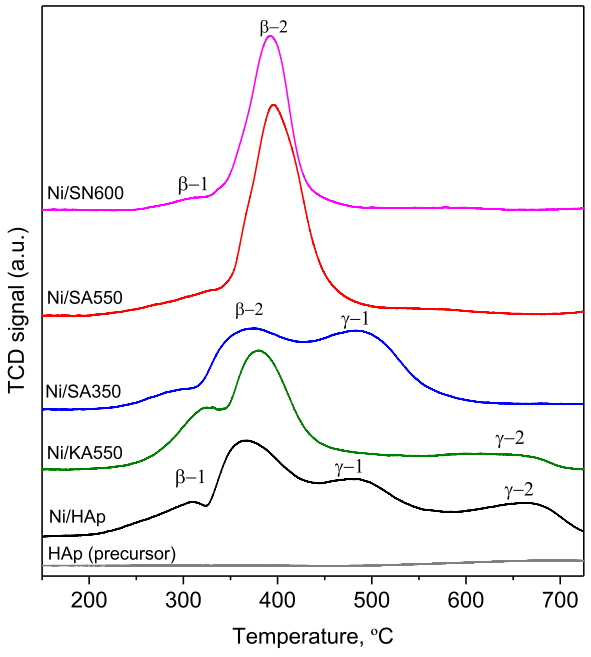

Fig. 3. Reduction profiles of selected catalysts.

The position of the reduction peaks and H_2 consumption values are listed in Table 3. It was observed that small NiO particles represented around 8 % (in moles) of the nickel loaded in the reference catalyst. The nickel was roughly distributed into equal parts in NiO particles with mild interaction with the support (β2-peak, 371 ºC) and ion exchanged species (γ1-peak, 470 ºC). Indeed, although the calcium nickel apatite phase could not be identified by XRD, the aforementioned lattice parameter values support the substitution of various ions in bioapatite. The reduction temperature of Ni^{2+} species in Ni/SA350 catalyst was similar to the reference catalyst, likely due to the similar HTT applied. The extremely high H_2 uptake of γ1-peak suggested that the dehydroxylation of the support took place at lower temperatures (around 482 ºC) as compared to the reference catalyst, coinciding with the ion exchanged $Ni^{\delta+}$ reduction range. This behaviour suggested that the acid treatment originated a more labile support, not sufficiently stabilized, due to the low HTT applied.

The increase of the HTT to 550 ºC or above, significantly modified the H_2 consumption profile. β2-peak increased by around 24 %, 56 % and 70 % for Ni/KA550, Ni/SA550 and Ni/SN600 catalysts, respectively, as compared to that of Ni/HAp. Moreover, the peak was centred at slightly higher temperature (ΔT_{max} ~ 11–27 ºC). These results evidence that the activation of the support produced a larger amount of bulk NiO in these three catalysts, and with a stronger metal-support interaction as compared to the reference catalyst (peak maximum shifted to higher temperature). The contribution of some ion exchanged $Ni^{\delta+}$ species or the existence of NiO particles located within the bioapatite channels should not be discarded. The greater amount of large pores in these chemically activated catalysts (Fig. 1) would support this hypothesis.

3.1.4. Surface characteristics

FTIR spectra (Fig. 4) confirmed the characteristic features of apatite with the fundamental vibrational modes of $\nu_1(PO_4^{3-})$ at around 962 cm^{-1}, ν_2 (PO_4^{3-}) at 474 cm^{-1}, ν_3 (PO_4^{3-}) at 1040–1090 cm^{-1} and ν_4 (PO_4^{3-}) at around 566 cm^{-1} and 603 cm^{-1} [44,45]. The bands at 633 cm^{-1} and 3572 cm^{-1} are characteristic of the stretching vibrations of OH^- groups in apatitic environment [46]. These latter bands were difficult to detect in the reference catalyst and those treated at HTT 350 ºC, suggesting that these catalysts contained poorly crystallized apatite, as confirmed by XRD. Moreover, carbonate features with a doublet at around 1450–1550 cm^{-1} and a singlet around 879 cm^{-1} were observed [47]. The broad shoulder at around 1480 cm^{-1} can be attributed to the presence of surface labile carbonate [48]. The thermal treatment increased the intensity of the characteristic bands of the apatite phase (i.e. the OH^- stretching bands at 633 cm^{-1} and 3572 cm^{-1} increased with

Table 3
H_2-TPR results of the most active catalysts. H_2 total uptake in $mmol_{H2}/g$, peak contribution in % of the loaded Ni.

Catalyst	H_2 total uptake [(1)]	Ni^{2+} species (β1-peak)	Ni^{2+} species (β2-peak)	Exchanged Ni^{2+} species (γ1-peak)	Dehydroxylation [(2)] (γ2-peak)
Ni/HAp	2.73 (1.92)	9.8 (281 °C)	53.4 (371 °C)	41.1 * (474 °C)	0.72 (560–652 °C)
Ni/KA550	1.93 (1.66)	19.5 (308 °C)	67.6 (384 °C)	11.4 (494 °C)	0.30 (615 °C)
Ni/SA350	2.56 (1.70)	11.6 (302 °C)	49.2 (374 °C)	78.3 * (482 °C)	0.19 (674 °C)
Ni/SA550	1.89 (1.66)	9.9 (303 °C)	86.9 (398 °C)	6.1 (456 °C)	0.18 (543 °C)
Ni/SN600	1.75 (1.66)	6.0 (308 °C)	96.0 (391 °C)	3.4 (455 °C)	n.d.

(1) In brackets, the theoretical uptake of the loaded nickel.
(2) In $mmol_{H2}/g$.
* Includes the reduction of exchanged Ni^{2+}, dehydroxylation and gasification.

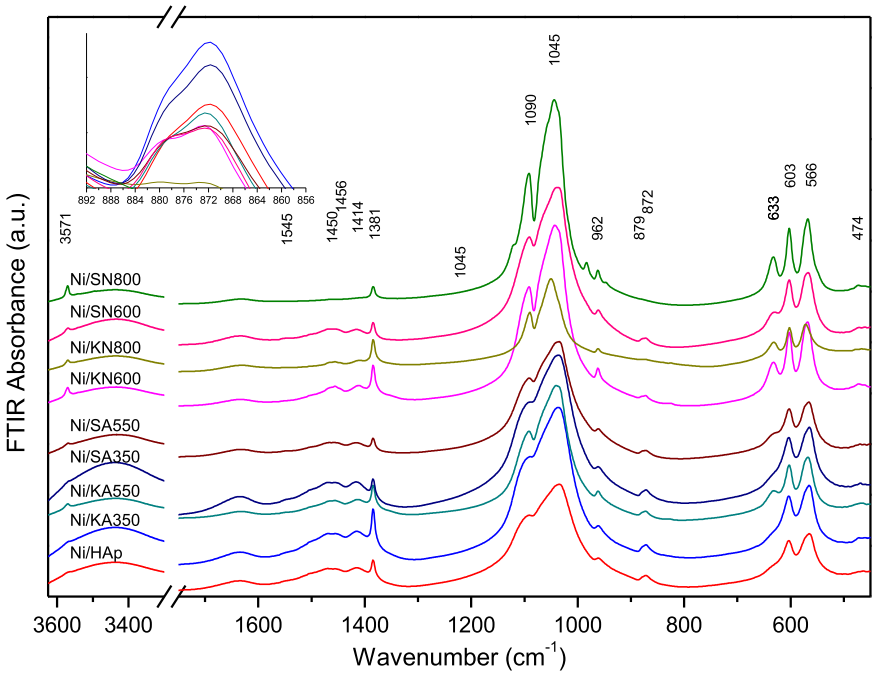

Fig. 4. FTIR spectra of catalysts of Ni supported on bone char.

HTT). This was likely due to the combined effect of the apatite crystallite growth and the removal of other constituents from the surface as temperature increased. Also, the main bending mode of the PO_4^{3-} at 1045 cm^{-1} was slightly red shifted what may be a signal that anions substituting OH^- in the apatite structure (i.e. F^-, CO_3^{2-}, etc.) were leached out [49,50]. The inverse relationship between the carbonate features and those corresponding to the apatitic OH^- groups supports the above idea. That is, samples where the signal of the apatitic OH^- groups at 3572 cm^{-1} was not observed showed more prominent features in the carbonate region.

The XPS survey scans (Table S3, Supplementary material) showed O, Ca and P as the most abundant elements in the as-prepared catalysts with a significant amount of C (i.e. 4.6–9.1 at %) and low amounts of other elements such as K, Na, Si, N, Cl. The surface concentration of K in the catalysts based on alkali-treated bone char increased (1.5 at %) whereas in the acid-treated catalysts decreased to 0.6 at % (pristine material: 1.0 at %), in accordance with the ICP results (Table S2, Supplementary material). This behaviour was more marked in the reduced

Table 4
XPS results of as prepared (calcined) and in-situ reduced catalysts. Units wt %.

Catalyst	As-prepared						Reduced				
	Ni [(1)]	Ni^{2+}/Ca^{2+} [(2)]	Ni 2p3/2 (eV)	Ni [(3)]	Ca/P	Ca/P bulk [(4)]	Ni [(1)]	Ni^{2+}/Ca^{2+} [(2)]	Ni 2p3/2 (eV)	Ni [(5)]	Ca/P
Ni/HAp	3.0	0.23	854.3/856.4	50	1.29	1.44	2.6	0.09	852.1/856.1	33	1.35
Ni/KA550	7.1	0.43	853.7/855.6	62	1.42	1.48	5.7	0.15	852.4/855.4	46	1.54
Ni/SA350	4.7	0.25	854.3/856.3	50	1.38	1.42	3.2	0.07	852.4/856.8	51	1.44
Ni/SA550	3.7	0.19	853.5/855.6	50	1.39	1.45	2.7	0.06	852.2/856.8	50	1.43
Ni/SN600	3.3	0.16	853.7/855.9	46	1.37	1.44	2.5	0.06	851.9/856.5	46	1.41

(1)Total Ni (wt %)
(2)atoms/atoms
(3)Relative amount of Ni^{2+} as NiO (wt %)
(4)ICP-AES
(5)Relative amount of metallic Ni (wt %)

catalysts, where the K content increased up to 3.9 at %. As expected, after the reduction the surface C content notably decreased in all samples (Table S4). Interestingly, the relative concentration of Ca and P atoms increased in the activated samples, which could be related to the surface enrichment in the apatitic phase after the activation of the supports. Moreover, the surface Ca/P atomic ratios (Table 4) were even lower than those measured by the bulk analysis. This could be due to either the substitution by ion exchange of the Ca^{2+} species in the apatite surface by Ni^{2+} or the existence of NiO particles that cover the surface sites of Ca. Among the treated samples, the surface Ca/P values were the lowest after acid activation. Furthermore, the relative atomic content of Ni on the surface was much lower than bulk content (i.e. around 3 at % for the pristine material, Table 4) which increased upon chemical treatment (i.e. up to 7.1 at % in calcined Ni/KA550).

The XPS data of both Ca 2p3/2 and O 1 S spectra are shown and discussed in Supplementary material (Fig. S6). Concerning the Ni 2p spectrum of the calcined catalysts (Fig. 5), a spin-orbit doublet at around 855 eV was observed, characteristic of Ni $2_{p3/2}$ [37,51]. The XPS spectra could be deconvoluted into two peaks, reflecting the existence of at least two different chemical environments of the Ni^{2+}cations, in line with the H_2-TPR profiles. The peak appearing at around 854 eV (and the broad satellite centred at around 861 eV) was attributed to NiO [52]. The peak at around 856 eV reflects the existence of nickel species in a more oxidized form. However, this peak cannot be assigned with complete certainty due to the complex main line splitting due to multiplet contributions in nickel oxides. It could also be assigned to Ni^{2+} ($Ni(OH)_2$) species (856.3 eV) [53] or Ni^{3+} species (NiOOH, OH-Ni-O-P in apatite) reported at around 856–857 eV [39,54]. The reference catalyst showed peaks at 854.3 eV and 856.4 eV. A major variation was found in the BE values for Ni/KA550, Ni/SA550 and Ni/SN600 catalysts (Table 4 and Fig. 5), whereas for Ni/SA350 the BE values were similar to those of the reference material.

After reduction at 400 ºC (Fig. 5), a BE near 852.4 eV appeared, characteristic of metallic Ni [55]. The NiO peak at 854.3 eV disappeared whereas that at around 856 eV could still be observed in all catalysts, reflecting the presence of $Ni^{\delta+}$ species with strong interaction with the support that were difficult to reduce. This peak appeared at the highest BE values for Ni/SA550 and Ni/SN600 catalysts (Table 4: 856.5–856.8 eV). Similarly to the variations found in TPR profiles (Fig. 3) it can be assigned to nickel species with a stronger Ni-support interaction (i.e. β2-peak at highest temperature). Contrarily, in Ni/KA550 catalyst it appeared at a lower BE of around 855.4 eV.

Moreover, XPS data revealed an equimolar amount of the two Ni 2p 3/2 species in the prepared (calcined) catalysts (Table 4). Ni/KA550 catalyst differed from the general trend, and showed a remarkable enrichment of Ni at the topmost layer (e.g. Ni/Ca atomic ratio of around 0.43), with 62 % of the loaded Ni being as free NiO at the surface. Consequently, Ni/KA550 catalyst contained the highest amount of metallic Ni (2.6 at %) upon reduction. Note that bulk Ni content for this sample was similar or even lower than that in the reference catalyst (Table 1: 9.7 vs. 11.3 wt %).

3.2. *WGS performance under ideal conditions*

Fig. 6 shows CO conversion as a function of temperature using an ideal reaction mixture. The reference catalyst Ni/HAp showed poor WGS activity up to 400 ºC ($X_{CO} \leq 27$ %). However, as temperature increased, the CO conversion rapidly reached 99.6 % at 425 ºC. This conversion was above equilibrium, indicating the occurrence of side reactions that consumed CO.

The activation of the support strongly modified the catalytic performance; the activity was enhanced in some cases whereas it was deteriorated in others. A first analysis of the light-off curves evidenced that the activation of biochar in inert atmosphere had a negative effect on the WGS performance (curves in Fig. 6A were shifted to the right). Catalysts based on K_2CO_3-treated biochars (Ni/KN600 and Ni/KN800)

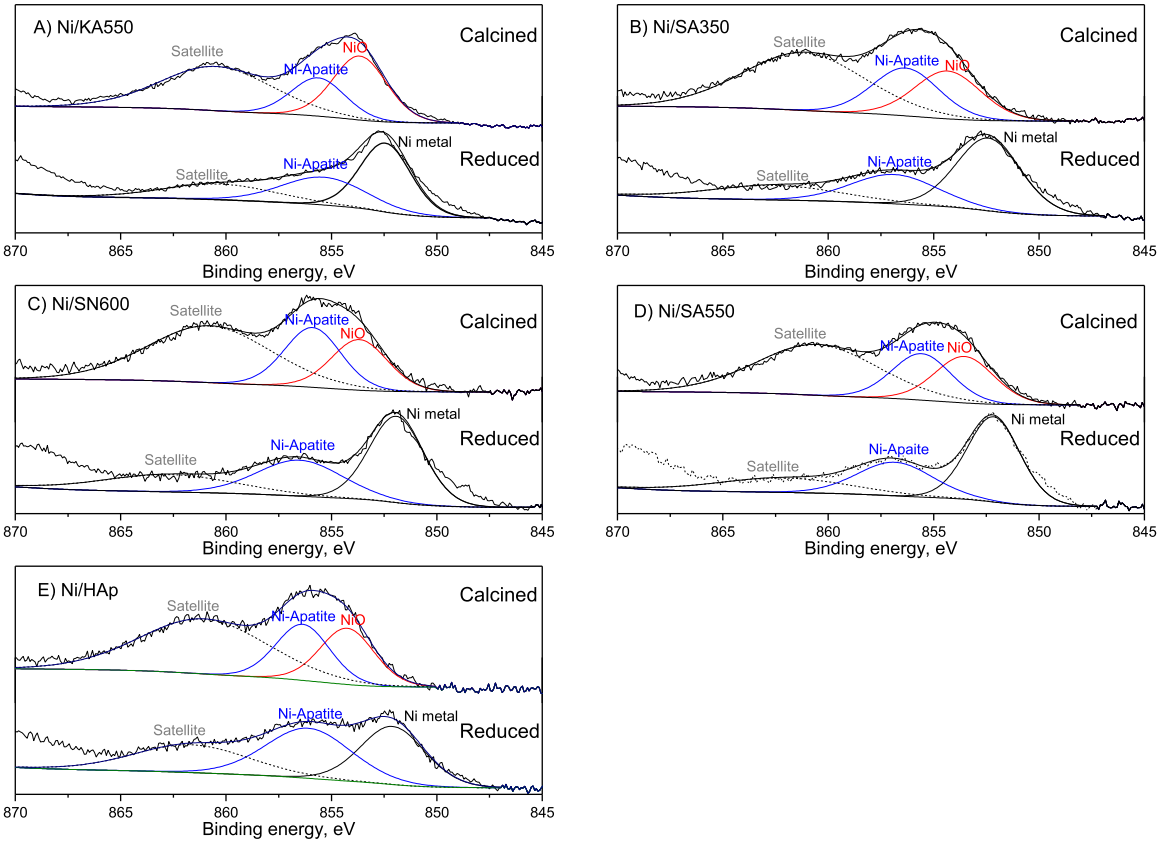

Fig. 5. XPS spectra of Ni 2p3/2 region of selected catalysts.

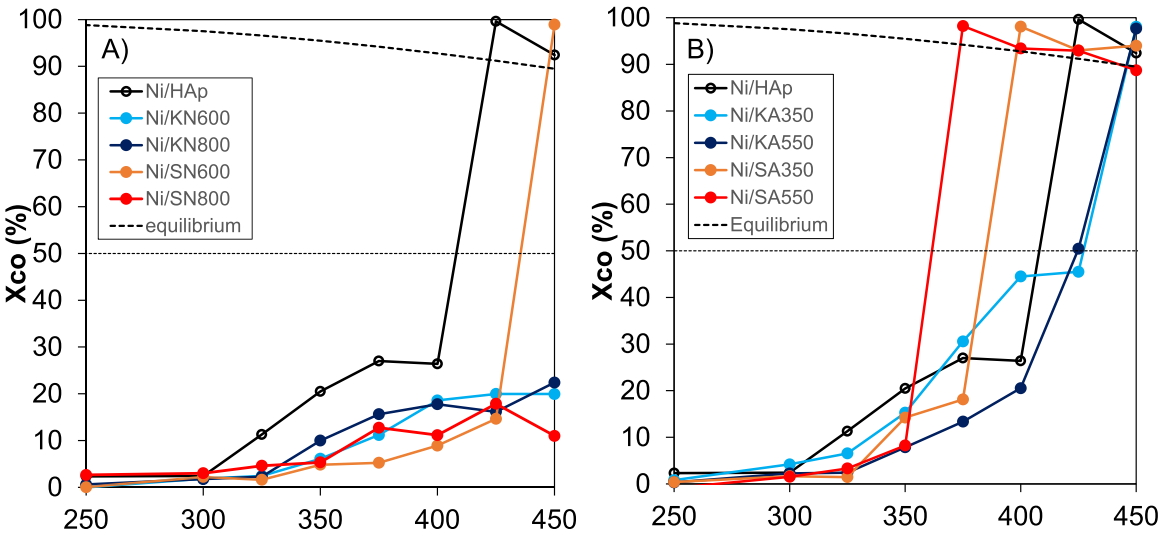

Fig. 6. Light-off curves for (A) Catalysts based on N_2-calcined biochar; (B) Catalysts based on air-calcined biochar. The 50 % conversion line is also depicted.

did not surpass 20 % CO conversion in all the temperature range, with little difference between them. Catalysts based on H_2SO_4-treated biochars (Ni/SN600, Ni/SN800) also showed poor catalytic performance ($X_{CO} \leq 10$ %) below 400 ºC. Only Ni/SN600 catalyst reached the equilibrium conversion, although at around 450 ºC. For this catalyst, the temperature for 50 % conversion (T_{50}), was about 25 ºC higher than that of reference Ni/HAp (Table 5).

The air-calcined catalysts showed the best WGS activity. Among them, the acid treatment improved the WGS activity (curves in Fig. 6B were shifted to the left). Likewise, the activity of the acid-treated catalysts increased with HTT. The T_{50} values (Table 5) varied as follows: Ni/SA550 < Ni/SA350 < Ni/HAp < Ni/KA550 ~ Ni/KA350. Hence, the most active catalyst (Ni/SA550) lowered the T_{50} value by around 50 ºC with respect to the reference catalyst. Note that all catalysts surpassed the equilibrium CO conversion in WGS, evidencing the occurrence of CO consuming side reactions.

Several representative results are shown in Table 5, including R_{CO} (specific reaction rate at 350 ºC, per gram of catalyst) and the apparent activation energy. The highest activity was obtained when Ni was supported on the pristine biochar (R_{CO} = 3.03 $\mu mol_{CO}/g_{cat}.s$). For similar HTT, the supports calcined in air atmosphere (Ni/KA550 and Ni/SA550) provided more active catalysts than those treated in inert atmosphere (Ni/KN600 and Ni/SN600): 28 % of increase for alkali treated samples and 74 % of increase for acid treated samples. The oxidizing atmosphere also lowered T_{50}, independent of the chemical activation used. The chemical activation significantly lowered the activation energy of the WGS reaction, especially in nitrogen atmosphere. For example, Ni/SN800 showed a three fold lower activation energy as compared to the reference Ni/HAp catalyst (46.8 vs 127.5 kJ/mol).

Table 5
Results of kinetic measurements for Ni catalysts supported on bone char.

Catalyst	Ideal conditions			Realistic conditions	
	T_{50} (ºC)	R_{CO} @ 350 ºC ($\mu mol_{CO}/g_{cat}.s$)	Ea (kJ/mol)	T_{50} (ºC)	Y_{CH4} (%) (1)
Ni/HAp	408	3.03	127.5	334	41.2 (350 ºC)
Ni/KA350	425	2.37	76.3	n/a	n/a
Ni/KA550	427	1.20	93.5	362	8.9 (375 ºC)
Ni/KN600	n/a	0.94	78.4	n/a	n/a
Ni/KN800	n/a	1.46	89.7	n/a	n/a
Ni/SA350	385	2.09	116.1	304	18.9 (325 ºC)
Ni/SA550	362	1.25	99.6	369	3.3 (425 ºC)
Ni/SN600	435	0.72	70.2	394	15.2 (n/a)
Ni/SN800	n/a	0.80	46.8	n/a	n/a

n/a non achieved; (1) methane yield at the minimum temperature for equilibrium (in brackets)

3.3. WGS under realistic conditions

The investigation was extended to realistic WGS conditions for the most active catalysts (Fig. 7). Ni/KA550, Ni/SA350, Ni/SA550 and Ni/SN600 catalysts were selected to allow the comparison between catalysts activated varying HTT, activating agent and heating atmosphere. The reference catalyst Ni/HAp was also included in the series. The results showed that changing the feed composition from ideal to realistic conditions the light-off curve downshifted between 41 and 81 ºC for Ni/HAp, Ni/KA550 and Ni/SA350 catalysts, i.e. catalysts were more active for CO conversion (for comparison, all curves are depicted in Fig. S2, Supplementary material). This behaviour could be attributed to the increased concentration of reactants in the feed, and suggests a positive reaction order for CO and H_2O [56]. In terms of CO conversion, Ni/SA350 catalyst was the most active. Actually, it was the unique catalyst that improved the activity of the reference catalyst (T_{50}: 334 ºC vs 304 ºC for Ni/HAp and Ni/SA350). The effect of feed composition on catalysts supported on bone char treated with acid at high HTT is interesting to note.

The activity of Ni/SA550 and Ni/SN600 catalysts was enhanced for the low temperature WGS (below 350 ºC); however, as temperature increased, the activity was deteriorated. For instance, switching the feed to realistic conditions, the T_{50} of Ni/SN600 was reduced by 41 ºC; nevertheless, the maximum CO conversion hardly surpassed 53 %.

Fig. 7B shows the evolution of methane yield with temperature. The most active catalysts (Ni/HAp and Ni/SA350) showed an extremely high methane formation (Y_{CH4} up to 49 % and 32 %, respectively), resulting in a negative H_2 net production (Fig. 7C).

That is, part of the H_2 fed was consumed in side reactions. The comparison of Ni/SA350 and Ni/SA550 catalysts is useful to analyse the effect of HTT on the methanation activity. As HTT was increased, the methanation was inhibited. Ni/SA550 catalyst provided the lowest methanation activity, yet it lacked of sufficient WGS activity (i.e. Y_{CH4}= 3.5 % and X_{CO} = 83 % at 450 ºC). Indeed, the main drawback of Ni

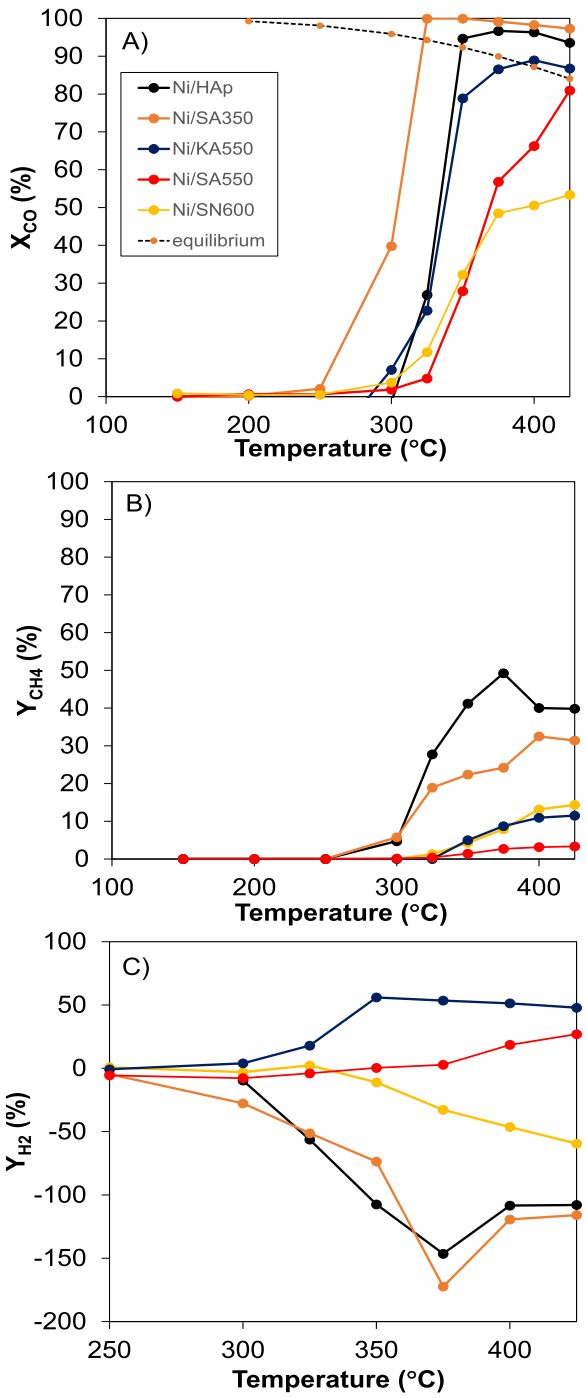

Fig. 7. WGS performance of selected Ni catalysts under reformer outlet stream conditions. Feed (in % vol.): $CO/H_2O/CO_2/H_2 = 5/46/4/31$, balance N_2. (A) Light-off curves; (B) Methane yield; (C) Hydrogen yield.

catalysts is their high activity for methane formation [57]. Among the most active catalysts, the lowest values of methane yield were measured for Ni/KA550. Among the strategies to reduce the methanation of Ni catalysts, the addition of alkaline metals such as K has proved to be effective [58]. The authors ascribed this behaviour to the increase of weakly basic OH^- groups on the modified catalyst. If the associative mechanism is applicable for the WGS reaction, a large amount of OH^- groups is important to form surface intermediate [59]. Indeed, potassium can supply active hydroxyl groups to the adsorbed CO species. In this context, it is hardly surprising that the alkali-treated catalyst (Ni/KA550) showed the most balanced catalytic behaviour. It reached the WGS equilibrium conversion at 400 °C ($X_{CO,eq} \sim 90$ %) with a six fold decrease in the methane yield as compared to the reference catalyst.

4. Discussion

According to the results, chemical activation modified the WGS performance. Taken into account the values of specific surface area and the catalytic results (Table 1 and Fig. 6), it seemed that the very low S_{BET} surface area of Ni/KN600, Ni/KN800 and Ni/SN800 catalysts hindered their WGS catalytic activity.

The results evidence an intense methanation activity for the reference catalyst ($Y_{CH4} = 49$ % at 375 ºC) during the WGS runs with H_2/CO_2 co-feeding, whereas in general, the methane yield of catalysts of Ni supported on bioapatite was reduced after activation. The high C content of the reference catalyst (9.2 wt %) compared to the chemically activated counterparts suggested that the hydrogenation of the carbonaceous material could represent an important source for CH_4 formation. The results showed that chemical activation removed the bulk carbonaceous content of support, especially at HTT = 550 ºC or above, suggesting that acid and alkali treatment swiped-off the carbonaceous residue on bone char [60].

Nevertheless, the surface carbonaceous content could not explain by itself the observed high variability in the WGS activity and selectivity of the catalysts. As an example, surface analysis revealed quite a similar C content in the reference catalyst Ni/HAp (1.5 at %) and other catalysts such as Ni/KA550 (1.1 at %), though with a five-fold difference in the methane production ($Y_{CH4} \sim 10$ vs. 50 % at 375 ºC). Analogously, Ni/SA550 and Ni/SN600 catalysts contained a similar carbon total content (0.4–0.5 wt %). The latter catalysts were prepared by thermal heating of the same specimen (the acid treated precursor) and showed comparable textural properties. Moreover, H_2-TPR data revealed a similar reducibility of Ni^{2+} species in these catalysts although heated under different atmosphere. However, Ni/SN600 catalyst showed poor WGS activity (it did not surpass 50 % CO conversion) with a negative hydrogen yield ($Y_{H2} = -59$ vs. 27 %, at 425 ºC) and five-fold larger methane formation than Ni/SA550 ($Y_{CH4} = 14.3$ vs. 3.2 %, at 425 ºC). Thus, the heating atmosphere has an important effect on the activity of the catalyst.

Regarding the effect of the atmosphere, the treatment in inert atmosphere possesses a negative effect on porosity. As previously discussed (Section 3.1.1.), at similar HTT, it yields catalysts with 20–56 % lower S_{BET} values. The better textural properties of samples activated in air atmosphere are attributed to the beneficial effect of the combustion reactions of carbon and hydrogen that take place during the thermochemical activation of the bioapatite support [12]. Moreover, the data of the same research suggest that the oxidizing atmosphere takes part in the generation of OH^- functional groups from the reaction of oxygen with hydrogen in the support. For example, in the case of SA550 and SN600 supports (used in this work to configure Ni/SA550 and Ni/SN600 catalysts), the ratio between the FTIR peak areas of OH^- and phosphate was larger for the former support (0.75 vs 0.57). Nevertheless, the FTIR data of the catalysts are not in good agreement with those of the supports (Fig. 8B). As will be discussed below, the transformation of the hydroxyl groups of bioapatite (both those existing in the apatite lattice and those formed during the activation step) to NiO during the calcination step would explain this phenomenon. The formed NiO sites would result in favourable active sites for the WGS reaction upon reduction.

Overall, Ni/SA550 and Ni/KA550 catalysts showed the best WGS performance, since the equilibrium CO conversion was attained with limited methane production, thus evidencing the beneficial effect of the oxidizing atmosphere. Indeed, these were the unique catalysts that provided a positive hydrogen yield at realistic conditions. Between both samples, the alkali treated catalyst showed, by far, the highest selectivity to hydrogen (Y_{H2} @400 ºC: 51.3 vs 18.5 %). It has been reported that the addition of alkaline metals onto bone char can improve the CO conversion with suppression of the methanation because of the increase in

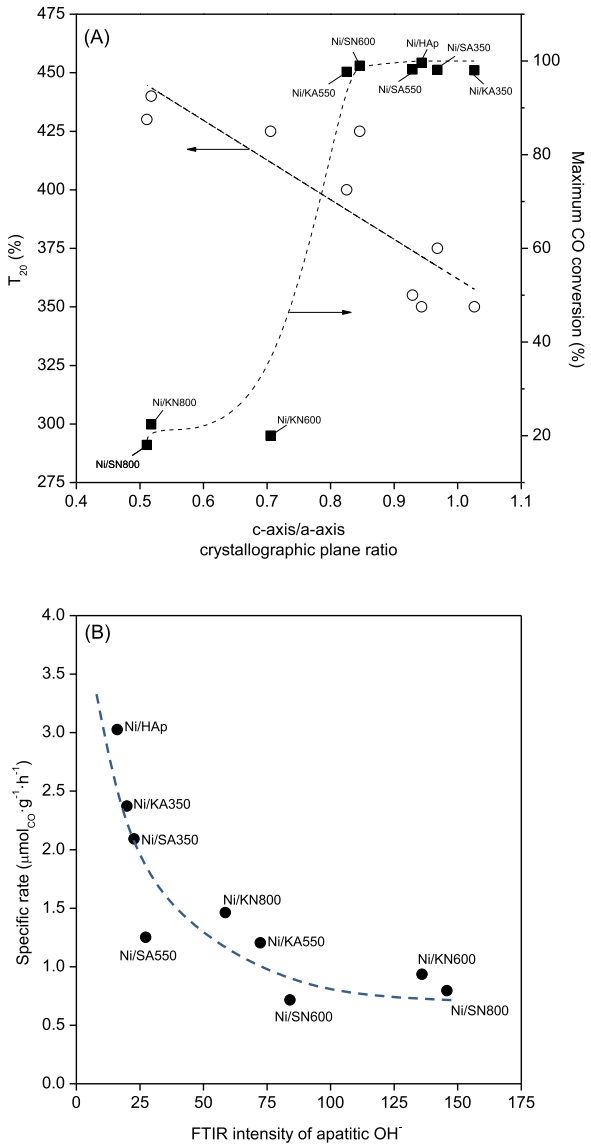

Fig. 8. WGS activity related to crystallographic characteristics, (A) Apatite crystal orientation from XRD. T_{20} (hollow symbol) X_{CO} (solid symbol); (B) Apatitic OH^- from FTIR at 3568 cm^{-1}.

weak basic sites [58,61]. NH_3-TPD analyses (Fig. S7, Supplementary material) indicated around two-fold decrease in the amount of acid sites in Ni/KA550 catalyst as compared to the reference sample (57.3 vs 117.9 $\mu mol_{NH3}/g$). In general, a positive correlation can be observed between acid-site density and methane yield [62]. Indeed, the treatment with K_2CO_3 reduced both the strength and the amount of acid sites. Since CO_2 and CO are slightly acidic and basic, respectively [63], a decreased acidity would facilitate the desorption of the as formed CO_2, before undergoing further hydrogenation to methane. It is known that CO_2 can be strongly adsorbed onto strong acid sites [64]. Moreover, a stronger binding of CO can result in hydrogenation to CH_4 [65]. The limitation of the methanation activity is an advantage of using naturally derived apatite, due to the presence of such alkalis in its composition even without chemical activation. XPS and EDS analyses confirmed the presence of low electronegativity heteroatoms (Na, K) at surface level (Tables S2 and S3, Supplementary material), which even increased upon reduction in hydrogen flow.

In order to explore in more detail the formation of methane, the Ni^0 crystallite size values were correlated with WGS performance (Table 3). It was observed that methane formation was the largest for catalysts with the smallest Ni^0 size (i.e. Ni/HAp, Ni/SA350). For non-reducible supports, since carbonyl is formed on metal surface, Ni^0 nanoparticles are identified as active sites for methanation [66]. However, the observed behaviour was contrary to that reported by others, in which CO_2 methanation activity increased with Ni^0 particle size [67]. Andersson et. al. [68] performed DFT and surface studies at ultra-high vacuum condition, and found that CO methanation mainly proceeds at under-coordinated sites such as step sites. This is because the energy barrier for CHO or CO dissociation on such sites are lower than closely-packed Ni (111) facet. Interestingly, the CO conversion increased with the relative abundance of horizontal reflection planes of the apatite phase in the support, as shown in Fig. 8A.

Fig. 8A shows a clear correlation in which the ignition temperature progressively decreased as the relative amount of *c*-axis facets in the apatite ($r_{c/a}$) increased. The maximum CO conversion showed a sigmoidal dependence with a threshold value of around $r_{c/a} = 0.7$. Catalysts with lower values of $r_{c/a}$ hardly surpassed 20 % CO conversion. From both indexes, a clear relation could be appreciated where the activation of CO molecule seemed to be favoured with the relative abundance of *c*-axis reflection planes of the apatite phase in the support. It is likely that a strong activation of the reactant molecules took place in specifically structured supports (i.e. non-stoichiometric apatite surfaces) [9]. Data in Table 2 suggested that $r_{c/a}$ was more severely affected by the heating atmosphere rather than by the chemical treatment.

XPS data highlighted the effect of the activation on surface characteristics. The chemical activation favoured the surface enrichment in Ni in both calcined and reduced form of the catalysts (Table 4). Moreover, the activation treatments increased the relative contribution of metallic Ni after the reduction (Table 4), which increased from around 33 % for the reference catalyst to around 50 % for the activated counterparts. The XPS spectra of the most WGS active catalysts in reduced form revealed an assignment of Ni $2_{p3/2}$ peak at around 856–857 eV ascribed to oxidized nickel species (i.e. Ni^{2+}/Ni^{3+} as $Ni(OH)_2$, NiOOH) [69]. For Ni/KA550 catalyst, this peak appeared at the lowest BE (i.e. around 855.4 eV), reflecting the existence of $Ni^{\delta+}$ species at intermediate oxidation state ($\delta < 2$), likely nickel species in an apatitic environment.

Interestingly, the WGS activity of the investigated catalysts increased as the amount of apatitic OH^- decreased (Fig. 8B). According to FTIR spectra, the signal of OH^- in the apatite at 633 and 3568 cm^{-1} was notably attenuated for the most active catalysts. Indeed, the transformation of the hydroxyl group of bioapatite to oxide has been previously reported by others [70]. This phenomenon can take place, leading to the transformation of most OH^- groups to NiO, which upon reduction would yield more favourable active sites for the WGS.

5. Conclusions

The chemical activation of bone char, used as support for Ni catalysts, allowed a superior WGS performance with a substantial decrease in the methane formation under real reformer conditions. Regarding the effect of the heating atmosphere, an inert atmosphere had a negative effect due to the collapse of the porous structure of support. Heating in air, on the contrary, improved the WGS activity and selectivity to H_2. Ni/KA550 catalyst showed the most balanced WGS performance: it reached the equilibrium conversion at 400 ºC with a six-fold decrease in the methane yield as compared to the non-activated reference catalyst.

The treatment with K_2CO_3 reduced both the strength and the amount of acid sites, thus leading to the suppression of methanation. The WGS activity increased with the relative abundance of horizontal facets of apatite crystals, which was more severely affected by the heating atmosphere than by the chemical treatment. It is hypothesized that the activation treatment, by increasing the pore volume and modifying the apatite crystal growing geometry, produced an important structural disorder and increased the number of defects in the surface of the support. This may facilitate the reducibility of NiO crystallites (formed partly from the transformation of the hydroxyl group of bioapatite) and

the subsequent surface enrichment in the metallic active phase.

The demonstrated potential of waste bone, available at large scale, as effective catalytic support can represent a promising solution to the growing environmental problems.

CRediT authorship contribution statement

Unai Iriarte-Velasco: Conceptualization, Funding acquisition, Investigation, Writing – original draft; **Irene Sierra**: Formal analysis, Writing – review & editing. **Miguel A. Gutiérrez-Ortiz**: Funding acquisition, Supervision. **Jose L. Ayastuy**: Conceptualization, Funding acquisition, Investigation.

Declaration of Competing Interest

The authors declare that they have no known competing financial interests or personal relationships that could have appeared to influence the work reported in this paper.

Data Availability

Data will be made available on request.

Acknowledgements

This work was supported by the Spanish Ministry of Economy and Competitiveness/Ministerio de Economía y Competitividad (PID2019-106692RB-I00) and the Basque Government (GV-2018-00038). The authors wish to express their gratitude for the technical and human support provided by SGIker of the UPV/EHU.

Appendix A. Supporting information

Supplementary data associated with this article can be found in the online version at doi:10.1016/j.jece.2023.110677.

References

[1] N.Z. Muradov, T.N. Veziroğlu, "Green" path from fossil-based to hydrogen economy: an overview of carbon-neutral technologies, Int J. Hydrog. Energy 33 (2008) 6804–6839.
[2] A.I. Osman, N. Mehta, A.M. Elgarahy, M. Hefny, A. Al-Hinai, A. Al-Muhtaseb, D. W. Rooney, Hydrogen production, storage, utilisation and environmental impacts: a review, Environ. Chem. Lett. 20 (2022) 153–188.
[3] T. Lepage, M. Kammoun, Q. Schmetz, A. Richel, Biomass-to-hydrogen: a review of main routes production, processes evaluation and techno-economical assessment, Biomass. Bioenergy 144 (2021), 105920.
[4] B. Dou, H. Zhang, Y. Song, L. Zhao, B. Jiang, M. He, C. Ruan, H. Chen, Y. Xu, Hydrogen production from the thermochemical conversion of biomass: issues and challenges, Sustain. Energy Fuels 3 (2019) 314–342.
[5] D.L. Trimm, Minimisation of carbon monoxide in a hydrogen stream for fuel cell application, Appl. Catal. A: Gen. 296 (2005) 1–11.
[6] D.B. Pal, R. Chand, S.N. Upadhyay, P.K. Mishra, Performance of water gas shift reaction catalysts: a review, Renew. Sustain. Energy Rev. 93 (2018) 549–565.
[7] G. Adduci, D. Martinez-Diaz, D. Sanz-Villanueva, A. Caravella, J.A. Calles, R. Sanz, D. Alique, Stability of electroless pore-plated Pd-membranes in acetic acid steam membrane-reformers for ultra-pure hydrogen production, Fuel Process Technol. 212 (2021), 106619.
[8] A. Venugopal, M.S. Scurrell, Hydroxyapatite as a novel support for gold and ruthenium catalysts: behaviour in the water gas shift reaction, Appl. Catal. A-Gen. 245 (2003) 137–147.
[9] D. Miao, A. Goldbach, H. Xu, Platinum/apatite water-gas shift catalysts, ACS Catal. 6 (2016) 775–783.
[10] V. Bolis, C. Busco, G. Martra, L. Bertinetti, Y. Sakhno, P. Ugliengo, F. Chiatti, M. Corno, N. Roveri, Coordination chemistry of Ca sites at the surface of nanosized hydroxyapatite: interaction with H_2O and CO, philosophical transactions: mathematical, Phys. Eng. Sci. 370 (2012) 1313–1336.
[11] A. Prévoteau, F. Ronsse, I. Cid, P. Boeckx, K. Rabaey, The electron donating capacity of biochar is dramatically underestimated, Sci. Rep. 6 (2016) 32870.
[12] I. Sierra, J.L. Ayastuy, M.A. Gutiérrez-Ortiz, U. Iriarte-Velasco, A study on the impact of the reaction mechanism of the thermochemical activation of bone char (by pyrolysis and carbonization), J. Anal. Appl. Pyrolysis 171 (2023), 105973.
[13] U. Iriarte-Velasco, I. Sierra, L. Zudaire, J.L. Ayastuy, Conversion of waste animal bones into porous hydroxyapatite by alkaline treatment: effect of the impregnation ratio and investigation of the activation mechanism, J. Mater. Sci. 50 (2015) 7568–7582.
[14] N. Medellin-Castillo, E. Padilla-Ortega, L.D. Tovar-García, R. Leyva-Ramos, R. Ocampo-Pérez, F. Carrasco-Marín, M. Berber-Mendoza, Removal of fluoride from aqueous solution using acid and thermally treated bone char, Adsorption 22 (2016) 951–961.
[15] ⟨https://ec.europa.eu/eurostat/statistics-explained⟩, 2022.
[16] U. Iriarte-Velasco, J.L. Ayastuy, Z. Boukha, R. Bravo, M.Á. Gutierrez-Ortiz, Transition metals supported on bone-derived hydroxyapatite as potential catalysts for the Water-Gas Shift reaction, Renew. Energy 115 (2018) 641–648.
[17] E. Dahdah, J. Estephane, C. Gennequin, A. Aboukaïs, S. Aouad, E. Abi-Aad, Effect of La promotion on Ni/Mg-Al hydrotalcite derived catalysts for glycerol steam reforming, J. Environ. Chem. Eng. 8 (2020), 104228.
[18] M.L. Ang, U. Oemar, Y. Kathiraser, E.T. Saw, C.H.K. Lew, Y. Du, A. Borgna, S. Kawi, High-temperature water–gas shift reaction over Ni/xK/CeO_2 catalysts: Suppression of methanation via formation of bridging carbonyls, J. Catal. 329 (2015) 130–143.
[19] M.L. Dieuzeide, M. Laborde, N. Amadeo, C. Cannilla, G. Bonura, F. Frusteri, Hydrogen production by glycerol steam reforming: How Mg doping affects the catalytic behaviour of Ni/Al_2O_3 catalysts, Int. J. Hydrog. Energy 41 (2016) 157–166.
[20] G.I. Siakavelas, N.D. Charisiou, S. AlKhoori, A.A. AlKhoori, V. Sebastian, S. J. Hinder, M.A. Baker, I.V. Yentekakis, K. Polychronopoulou, M.A. Goula, Highly selective and stable nickel catalysts supported on ceria promoted with Sm_2O_3, Pr_2O_3 and MgO for the CO_2 methanation reaction, Appl. Catal. B: Environ. 282 (2021), 119562.
[21] K. Rubin, A. Pohar, Venkata Dasireddy, D.B.C., B. Likozar, Synthesis, characterization and activity of CuZnGaOx catalysts for the water–gas shift (WGS) reaction for H2 production and CO removal after reforming, Fuel Process Technol. 169 (2018) 217–225.
[22] U. Iriarte-Velasco, J.L. Ayastuy, R. Bravo, Z. Boukha, M.A. Gutiérrez-Ortiz, Biogenic hydroxyapatite as novel catalytic support for Ni and Cu for the water–gas shift reaction, J. Mater. Sci. 56 (2021) 6745–6763.
[23] M. Šljivić-Ivanovič, I. Smičiklas, B. Milenković, B. Dojčinović, B. Babić, M. Mitrić, Evaluation of the effects of treatment factors on the properties of bio-apatite materials, J. Mater. Sci. 50 (2015) 354–365.
[24] K. Zhao, B. Qiao, Y. Zhang, J. Wang, The roles of hydroxyapatite and FeOx in a Au/FeOx hydroxyapatite catalyst for CO oxidation, Chin. J. Catal. 34 (2013) 1386–1394.
[25] H.M.H. Gad, M.A. Youssef, Sorption behavior of Eu(III) from an aqueous solution onto modified hydroxyapatite: kinetics, modeling and thermodynamics, Environ. Technol. 39 (2018) 2583–2596.
[26] L. Yami Teshome, F. Chamberlain Jim, C. Butler Elizabeth, A. Sabatini David, Using a high-capacity chemically activated cow bone to remove fluoride: field-scale column tests and laboratory regeneration studies, J. Environ. Eng. 143 (2017) 04016083.
[27] H. Abd-Rabboh, K. Fawy, N. Awwad, Removal of copper(II) from aqueous samples using natural activated hydroxyapatite sorbent produced from camel bones, Desalin. Water Treat. 164 (2019) 300–309.
[28] M.J. Amiri, A. Faraji, M. Azizi, B.G. Nejad, M. Arshadi, Recycling bone waste and cobalt-wastewater into a highly stable and efficient activator of peroxymonosulfate for dye and HEPES degradation, Process Saf. Environ. Prot. 147 (2021) 626–641.
[29] Y. Sa, Y. Guo, X. Feng, M. Wang, P. Li, Y. Gao, X. Yang, T. Jiang, Are different crystallinity-index-calculating methods of hydroxyapatite efficient and consistent? N. J. Chem. 41 (2017) 5723–5731.
[30] S. Wei, H. Zhang, Y. Huang, W. Wang, Y. Xia, Z. Yu, Pig bone derived hierarchical porous carbon and its enhanced cycling performance of lithium-sulfur batteries, Energy Environ. Sci. 4 (2011) 736–740.
[31] X. Wei, Y. Wang, X. Li, R. Wu, Y. Zhao, Co_3O_4 supported on bone-derived hydroxyapatite as potential catalysts for N_2O catalytic decomposition, Molecular, Catalysis 491 (2020), 111005.
[32] S. Patel, J. Han, W. Qiu, W. Gao, Synthesis and characterisation of mesoporous bone char obtained by pyrolysis of animal bones, for environmental application, J. Environ. Chem. Eng. 3 (2015) 2368–2377.
[33] F. Hussain, S. Alshahrani, M.M. Abbas, H.M. Khan, A. Jamil, H. Yaqoob, M.E. M. Soudagar, M. Imran, M. Ahmad, M. Munir, Waste animal bones as catalysts for biodiesel production; a mini review, Catalysts 11 (2021).
[34] D. Pham Minh, H. Sebei, A. Nzihou, P. Sharrock, Apatitic calcium phosphates: synthesis, characterization and reactivity in the removal of lead(II) from aqueous solution, Chem. Eng. J. 198–199 (2012) 180–190.
[35] T.S. Phan, A.R. Sane, B.R. de Vasconcelos, A. Nzihou, P. Sharrock, D. Grouset, D. P. Minh, Hydroxyapatite supported bimetallic cobalt and nickel catalysts for syngas production from dry reforming of methane, Appl. Catal. B: Environ. 224 (2018) 310–321.
[36] Y. Wang, X. Hu, K. Zheng, X. Wei, Y. Zhao, Effect of SnO_2 on the structure and catalytic performance of Co_3O_4 for N_2O decomposition, Catal. Commun. 111 (2018) 70–74.
[37] A. Belhadi, S. Boumaza, A. Djadoun, M. Trari, O. Cherifi, Methane steam reforming on supported nickel, effect of nickel content for product hydrogen, Open, J. Phys. Chem. 06 (2016) 34–41.
[38] H.V. Fajardo, E. Longo, D.Z. Mezalira, G.B. Nuernberg, G.I. Almerindo, A. Collasiol, L.F.D. Probst, I.T.S. Garcia, N.L.V. Carreño, Influence of support on catalytic behavior of nickel catalysts in the steam reforming of ethanol for hydrogen production, Environ. Chem. Lett. 8 (2010) 79–85.
[39] J.H. Jun, T. Lee, T.H. Lim, S. Nam, S. Hong, K.J. Yoon, Nickel–calcium phosphate/hydroxyapatite catalysts for partial oxidation of methane to syngas: characterization and activation, J. Catal. 221 (2004) 178–190.

[40] F. Mesrar, M. Kacimi, L.F. Liotta, F. Puleo, M. Ziyad, Hydrogen production on Ni loaded apatite-like oxide synthesized by dissolution-precipitation of natural phosphate, Int. J. Hydrog. Energy 42 (2017) 19458–19466.
[41] M.O. Abba, V.M. Gonzalez-DelaCruz, G. Colón, S. Sebti, A. Caballero, In situ XAS study of an improved natural phosphate catalyst for hydrogen production by reforming of methane, Appl. Catal. B: Environ. 150–151 (2014) 459–465.
[42] Y. Liu, Z. Shen, Dehydroxylation of hydroxyapatite in dense bulk ceramics sintered by spark plasma sintering, J. Eur. Ceram. Soc. 32 (2012) 2691–2696.
[43] W. Li, Z. Yu, G. Guan, Catalytic coal gasification for methane production: a review, Carbon Resour. Convers. 4 (2021) 89–99.
[44] J.C. Elliott, Structure and Chemistry of the Apatites and Other Calcium Orthophosphates, Elsevier, 2013.
[45] C. Drouet, Apatite formation: why it may not work as planned, and how to conclusively identify apatite compounds, BioMed. Res. Int. 2013 (2013), 490946.
[46] S.S.A. Abidi, Q. Murtaza, Synthesis and characterization of nano-hydroxyapatite powder using wet chemical precipitation reaction, J. Mater. Sci. Technol. 30 (2014) 307–310.
[47] H. Madupalli, B. Pavan, M.M.J. Tecklenburg, Carbonate substitution in the mineral component of bone: discriminating the structural changes, simultaneously imposed by carbonate in A and B sites of apatite, J. Solid State Chem. 255 (2017) 27–35.
[48] A.C. Deymier, A.K. Nair, B. Depalle, Z. Qin, K. Arcot, C. Drouet, C.H. Yoder, M. J. Buehler, S. Thomopoulos, G.M. Genin, Protein-free formation of bone-like apatite: new insights into the key role of carbonation, Biomaterials 127 (2017) 75–88.
[49] D. Miao, G. Cavusoglu, H. Lichtenberg, J. Yu, H. Xu, J. Grunwaldt, A. Goldbach, Water-gas shift reaction over platinum/strontium apatite catalysts, Appl. Catal. B: Environ. 202 (2017) 587–596.
[50] J. Terra, E.R. Dourado, J. Eon, D.E. Ellis, G. Gonzalez, A.M. Rossi, The structure of strontium-doped hydroxyapatite: an experimental and theoretical study, Phys. Chem. Chem. Phys. 11 (2009) 568–577.
[51] M. Lenglet, F. Hochu, J. Dürr, M.H. Tuilier, Investigation of the chemical bonding in 3d8 nickel(II) charge transfer insulators (NiO, oxidic spinels) from ligand-field spectroscopy, Ni 2p XPS and X-ray absorption spectroscopy, Solid State Commun. 104 (1997) 793–798.
[52] M.A. Peck, M.A. Langell, Comparison of nanoscaled and bulk NiO structural and environmental characteristics by XRD, XAFS, and XPS, Chem. Mater. 24 (2012) 4483–4490.
[53] M. Akri, S. Zhao, X. Li, K. Zang, A.F. Lee, M.A. Isaacs, W. Xi, Y. Gangarajula, J. Luo, Y. Ren, Y. Cui, L. Li, Y. Su, X. Pan, W. Wen, Y. Pan, K. Wilson, L. Li, B. Qiao, H. Ishii, Y. Liao, A. Wang, X. Wang, T. Zhang, Atomically dispersed nickel as coke-resistant active sites for methane dry reforming, Nat. Commun. 10 (2019) 5181.
[54] Z. Boukha, M. Kacimi, M.F.R. Pereira, J.L. Faria, J.L. Figueiredo, M. Ziyad, Methane dry reforming on Ni loaded hydroxyapatite and fluoroapatite, Appl. Catal. A-Gen. 317 (2007) 299–309.
[55] E. Kordouli, B. Pawelec, C. Kordulis, A. Lycourghiotis, J.L.G. Fierro, Hydrodeoxygenation of phenol on bifunctional Ni-based catalysts: Effects of Mo promotion and support, Appl. Catal. B: Environ. 238 (2018) 147–160.
[56] H. Su, C. Yu, J. Liu, Y. Zhao, X. Ma, J. Luo, C. Sun, W. Li, K. Sun, CO activation and methanation mechanism on hexagonal close-packed Co catalysts: effect of functionals, carbon deposition and surface structure, Catal. Sci. Technol. 10 (2020) 3387–3398.
[57] K. Jalama, Carbon dioxide hydrogenation over nickel-, ruthenium-, and copper-based catalysts: Review of kinetics and mechanism, Catal. Rev. 59 (2017) 95–164.
[58] K. Hwang, C. Lee, J. Park, Advanced nickel metal catalyst for water–gas shift reaction, J. Power Sources 196 (2011) 1349–1352.
[59] Y. Cui, Z. Li, Z. Zhao, V.J. Cybulskis, K.D. Sabnis, C.W. Han, V. Ortalan, W. F. Schneider, J. Greeley, W.N. Delgass, F.H. Ribeiro, Participation of interfacial hydroxyl groups in the water-gas shift reaction over Au/MgO catalysts, Catal. Sci. Technol. 7 (2017) 5257–5266.
[60] I. Sierra, U. Iriarte-Velasco, J.L. Ayastuy, A.T. Aguayo, Production of magnetic sewage sludge biochar: investigation of the activation mechanism and effect of the activating agent and temperature, Biomass. Convers. Biorefinery (2022).
[61] F. Meshkani, M. Rezaei, Hydrogen production by high temperature water gas shift reaction over highly active and stable chromium free Fe-Al-Ni catalysts, Int. J. Hydrog. Energy 40 (2015) 10867–10875.
[62] H. Wang, Y. Pei, M. Qiao, B. Zong, Advances in methanation catalysis, Anon. Catal.: Vol. 29, R. Soc. Chem. (2017) 1–28.
[63] M.D. Porosoff, J.G. Chen, Trends in the catalytic reduction of CO_2 by hydrogen over supported monometallic and bimetallic catalysts, J. Catal. 301 (2013) 30–37.
[64] S. Andonova, C.N. de Ávila, K. Arishtirova, J.M.C. Bueno, S. Damyanova, Structure and redox properties of Co promoted Ni/Al_2O_3 catalysts for oxidative steam reforming of ethanol, Appl. Catal. B: Environ. 105 (2011) 346–360.
[65] M. Juneau, C. Pope, R. Liu, M.D. Porosoff, Support acidity as a descriptor for reverse water-gas shift over Mo2C-based catalysts, Appl. Catal. A: Gen. 620 (2021), 118034.
[66] F. Wang, S. He, H. Chen, B. Wang, L. Zheng, M. Wei, D.G. Evans, X. Duan, Active site dependent reaction mechanism over Ru/CeO_2 catalyst toward CO_2 methanation, J. Am. Chem. Soc. 138 (2016) 6298–6305.
[67] L. Lin, C.A. Gerlak, C. Liu, J. Llorca, S. Yao, N. Rui, F. Zhang, Z. Liu, S. Zhang, K. Deng, C.B. Murray, J.A. Rodriguez, S.D. Senanayake, Effect of Ni particle size on the production of renewable methane from CO_2 over Ni/CeO_2 catalyst, J. Energy Chem. 61 (2021) 602–611.
[68] M.P. Andersson, F. Abild-Pedersen, I.N. Remediakis, T. Bligaard, G. Jones, J. Engbæk, O. Lytken, S. Horch, J.H. Nielsen, J. Sehested, J.R. Rostrup-Nielsen, J. K. Nørskov, I. Chorkendorff, Structure sensitivity of the methanation reaction: H_2-induced CO dissociation on nickel surfaces, J. Catal. 255 (2008) 6–19.
[69] A.P. Grosvenor, M.C. Biesinger, R.S.C. Smart, N.S. McIntyre, New interpretations of XPS spectra of nickel metal and oxides, Surf. Sci. 600 (2006) 1771–1779.
[70] A. Grunenwald, C. Keyser, A.M. Sautereau, E. Crubézy, B. Ludes, C. Drouet, Revisiting carbonate quantification in apatite (bio)minerals: a validated FTIR methodology, J. Archaeol. Sci. 49 (2014) 134–141.